ORIGINAL ARTICLE

A novel underactuated smart surface for parts feeding and sorting

Edoardo Bianchi[1] · Gualtiero Fantoni[2] · Francisco Javier Brosed Dueso[1] · José A. Yagüe-Fabra[1]

Abstract

In material handling, numerous solutions have been proposed to enhance the flexibility and adaptability of transport systems. Among these solutions, smart surfaces stand out as one of the most interesting responses, utilizing an array of actuators for common feeding tasks. The current paper focuses on a novel system within this category, notable for its distinguishing factor of being underactuated. With this characteristic, the concept leads to a simplified cost-effective design and a not actively driven functioning, leveraging gravity or object own velocity to manipulate the material flow maintaining top class performances, as the sorting rate reaches 4000 pcs/h. Specifically, the article begins with an introduction of the concept design and its digital model, followed by a description of the experimental setup built to test the surface's functionality and evaluate the predictions of the virtual counterpart. On top of that, a method to determine the essential parameters for the surface simulation is proposed and applied. As a result, the prototype successfully completed the three main intralogistic tasks experimented, i.e., sorting, slowing, and stopping of packages. Lastly, the digital model outcomes of the same operations were computed and compared with the measured results, demonstrating an accuracy of prediction with displacements and time errors below 7%.

1 Introduction

The study of material handling and transportation efficiency in industrial and warehouse contexts is a recurring theme in scientific research, driven by the market's demand for enhanced flexibility [1, 2]. A recent response to these demands is a class of systems called smart surfaces (sometimes also active surfaces) [3–5], i.e., programmable arrays of actuators capable of creating force fields.

These distributed manipulators are utilized in activities such as positioning, diverting, sorting, orienting, and feeding parts along a transfer line or a conveyance system, ultimately directing them towards a manufacturing system or a warehouse. Amidst the technologies applied to realize these devices, the most relevant ones exploit micro electromechanical systems (MEMS) [6, 7], vibrations [8, 9], ciliary motion [10–12], air [13, 14], variable morphology [15, 16], mobile platforms [17, 18], and rotors [19, 20]. Each one of these classes has its own advantages and field of application. Specifically, starting from the first, MEMS were one of the earliest ideas for the distributed manipulation of small and minuscule parts using micro cantilevers [7] or tilting planes [6, 21]. Secondly, the vibrations also are interesting for orienting and feeding light and compact objects. Precisely, they exploit the control of vibration frequencies of a planar sheet [8] or multiple minor planes [9]. Thirdly, ciliary surfaces can be used to manipulate delicate objects at low speeds using bio-inspired, rotating [10] or bending, cantilevers (cilia) [11, 12]. Pneumatic systems are probably the most studied technology among smart surfaces; because of this, there are many solutions [13] proposing air jets [3, 22] or pressure fields [14, 23] for a contactless handling of

✉ Edoardo Bianchi
  ebianchi@unizar.es

  Gualtiero Fantoni
  gualtiero.fantoni@unipi.it

  Francisco Javier Brosed Dueso
  fjbrosed@unizar.es

  José A. Yagüe-Fabra
  jyague@unizar.es

1 Department of Design and Manufacturing Engineering, I3A, University of Zaragoza, C/ Maria de Luna 3, Zaragoza, 50018 Zaragoza, Spain

2 Department of Civil and Industrial Engineering, University of Pisa, Largo Lucio Lazzarino, 56122 Pisa, Italy

micro- and macroscopic parts. Not very differently from the ciliary surfaces, the variable morphology ones alter their shape through linear actuators or inflatable chambers to carry small-sized and light materials. Instead, the mobile platform class is a bordering solution for smart surfaces, as does have an intermediate body below [17, 18] or around [24] the object transported, allowing its motion without axis restrictions in a confined area. Finally, the rotor technology is mostly employed to handle packages within logistical operations, because of the capability to bear heavy loads and achieve higher speeds with modular arrays of spinning rotors [19, 20].

Eventually, the current paper focuses on the last of the smart surfaces' families, i.e., the rotors one. Many examples of these systems can be found in the literature [19, 20, 25–29] and among patents [30, 31]. Evaluating them one by one, the authors noticed two main groups of solutions differentiated by the characteristics of the single module. The first group proposes basic units with many motorized omnidirectional wheels with a fixed orientation for the rotation axis. Among the solutions, there are modules with a minimum of two motors [29] up to three [19, 25] or even four in some cases [20]. A cell of this sort generates on the object transported an overall friction force resulting by the sum of each wheel contributes. These components are influenced by the spinning velocity and are directed mainly perpendicularly to the rotor axis because of the reduced friction of omnidirectional wheels. On the other side, the second group of basic units [27, 28] employs a single rotor per module, with two motorized axes, i.e., one perpendicular to the surface plane and the other driving the rotor. Specifically, the first axis steers the wheel in the plane, while the second controls the spinning velocity.

Overall, both these solutions appear to have high handling capabilities and, accordingly, important performance. However, as highlighted in the previous paragraph, all the proposals involve several motors (at least two) per surface unit in order to complete their tasks. This aspect may complicate the design and the maintenance and increase the costs in terms of money and control effort.

On the other end, what is missing in the literature is an underactuated version that exploits other motion input sources, e.g., gravity [12] or previous object's velocity, to achieve the same goals with a simpler design and without using motors. In this context, the paper addresses a novel system with these characteristics, while remaining within the rotors class and ensuring uncompromised performance. The aim is to reduce costs and energy consumption, aligning with what is observed in numerous other underactuated robotic systems [32].

The resulting surface is an array of autonomously programmable modules where, in each one, a spherical rotor is controlled through its rotation axis (steering) to create a friction force field. Additionally, the modules do not contain motors, and the sphere axis of rotation can assume only a discrete number of positions to further simplify the design.

The paper covers with a brief introduction of the single unit functioning and design. The focus then moves to presenting the digital model of the same concept, expanded to a larger scale and capable of simulating surface behavior under various conditions. Therefore, the experimental setup of the depicted surface is described from its hardware to the planned operation. Practically, the framework is built for testing the functioning during sorting, slowing, and stopping operations of packages, and for evaluating the accuracy of the digital model described. Therefore, with the assessment of the prediction goodness, the performances of the device are easier to identify as they can be computed by simulation. This permits a comparison of the concept object of the study with similar systems in terms of sorting capacity, proving a satisfactory sorting rate despite the underactuation. Finally, the work presents a further improvement to the system's flexibility, i.e., an auto configuration process that can be used to detect in a real environment the parameters necessary for the simulation outcomes according to the operational conditions. In other terms, the digital model adjusts to physical changes in transported parts, expanding the application of the system to a wider range of parcels and scenarios beyond those outlined in the paper.

The outline of the remaining part of the paper is the following: Section 2 briefly introduces the concept design and its digital model, Section 3 presents the experimental setup built to test the surface and the measurements planned, Section 4 reports the results of the testing and the evaluation of the digital model, while, lastly, Section 5 consists of the conclusions.

2 Concept description

2.1 Concept design

This study explores a novel modular surface for material handling along transport lines. The array units constituting the setup can be assembled according to the dimensions of the material transported and the handling purpose. Additionally, each module can act independently from the others to further increase the flexibility and adaptability of the system. Figure 1(a) depicts a schematic representation of this surface in a generic layout along with the reference coordinates for a transported object.

Moving on to the single module, its design is simpler and newer compared to systems of the same category; in fact, it does not involve motors and leverages the efficiency advantages inherent in an underactuated design. Its functioning exploits external input sources, e.g., gravity, previous
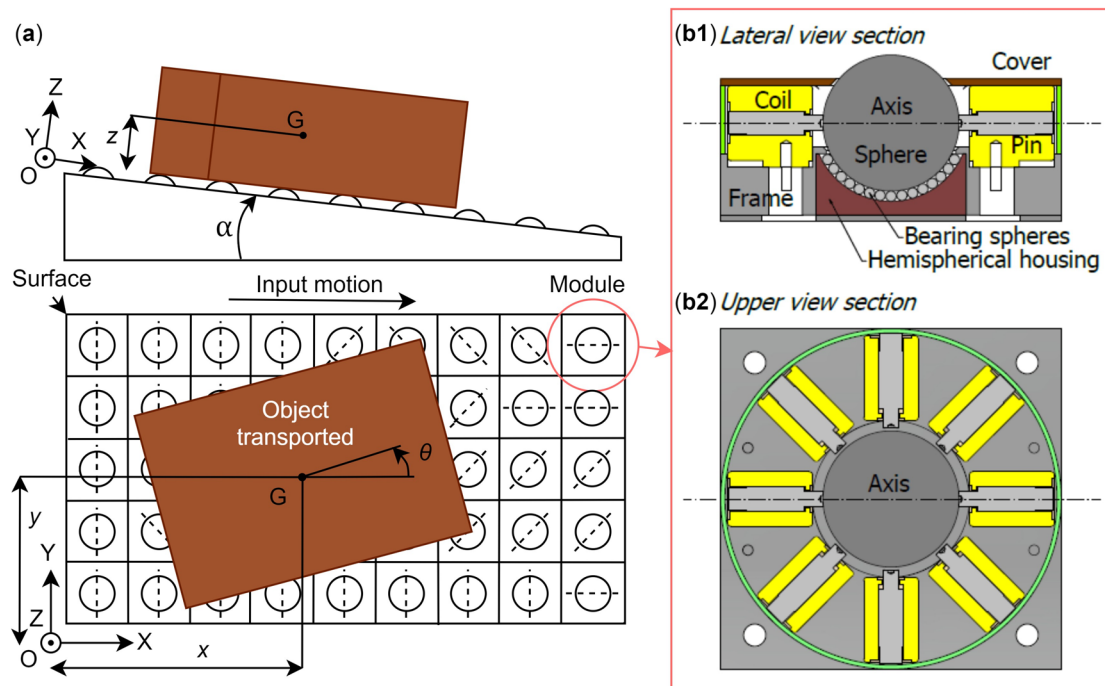
Fig. 1 Schematic representation of (**a**) a generic surface layout and (**b1**) the lateral and (**b2**) the upper view sections of the single module prototype.

velocity of the transported object, or a combination of both to compensate the missing actuation, placing the system within the class of not actively driven devices. In Fig. 1(b1) and (b2), both lateral and upper sections of the module prototype built for the experimental setup and its main components are displayed. Each module consists of a main sphere, supported by a hemispheric housing with bearings spheres and surrounded in its middle plane by electromagnets with pins inside. In total, the pins are 8 for this prototype; therefore, 4 axis orientations are available ([0°, 45°, 90°, 135°]). The device is actuated solely by defining the sphere's axis of rotation through the mentioned pins. Specifically, when the axis direction is selected, the pair of opposite pins defining that direction attaches to the sphere thanks to their magnetization produced by the coils. The friction forces generated by this contact support temporarily the axis until a new direction is selected or the device is turned off.

A rotor thus defined, when it is in contact with an object moving above it, exchanges two main friction forces: a prevailing one, parallel to the axis of rotation, and a minor one, perpendicular to the same axis. These two components constitute the punctual characteristics of the force field used for the material flow manipulation. In [33], the module functioning and its components are extensively explained. Additionally, the analytic model of these forces is experimentally validated, revealing two primary friction coefficients (μ_{max}, μ_{min}) as the main parameters describing them. The first one, μ_{max}, is the normal friction coefficient between the sphere

and the object transported (no distinction between static and dynamic), while the second, μ_{min}, models the resistance of the rotor when is spinning around its axis. Considering now the whole surface as an arrangement of modules, and therefore as an array of points associated with friction forces pairs, the force field results in its entirety. The effect of these components' interaction on an object is investigated in [34], where this analysis is used to create a digital model of the surface that can be used to simulate and predict its behavior. This virtual counterpart of the surface has been validated in [34] through a comparison with a dynamic simulation software, showcasing various applications and theoretical performances of the surface. However, an experimental validation of the system is missing to confirm the outcomes of the digital model with real data. The current study aims to fill this gap and to refine with experimental values the results computable with the digital model.

2.2 Concept digital model

Therefore, since one goal of this work is to validate experimentally this simulation environment, its logic and formulation will be briefly summarized in this section. Nevertheless, for an extensive explanation, the readers are invited to refer to [34].

The software used to build this virtual counterpart was *Matlab* and *Simulink* (*R2022b*), where all the analytic models were implemented. Specifically, the models concern

the single module and the object dynamics together with the contact friction between them. The procedure used to reproduce the motion of an object follows the actions of the flowchart depicted in Fig. 2. Before starting, as step zero (**S0** in Fig. 2), some input data regarding the object and the surface (geometry, inertia, friction, layout, and external motion input) have to be set up. Once the initial condition is defined, the loop starts iterating these steps, i.e., **S1**, **S2**, **S3**, **S4**, and **S5** of Fig. 2:

S1. The rotors momentarily in contact with the object are detected using the initial position of the object center of mass (G), the known geometry of the object, and the surface layout;

S2. All the forces acting on the object are computed, considering the object's weight distribution on the modules, the velocity on the contact points, and the friction model together. Therefore, the interaction of these forces determines the body equilibrium and its acceleration;

S3. The condition of motion for the object is evaluated. This is based on the position of the object above the modules' grid, its velocity (positive, null, or negative), the friction forces acting, and the inclination of the
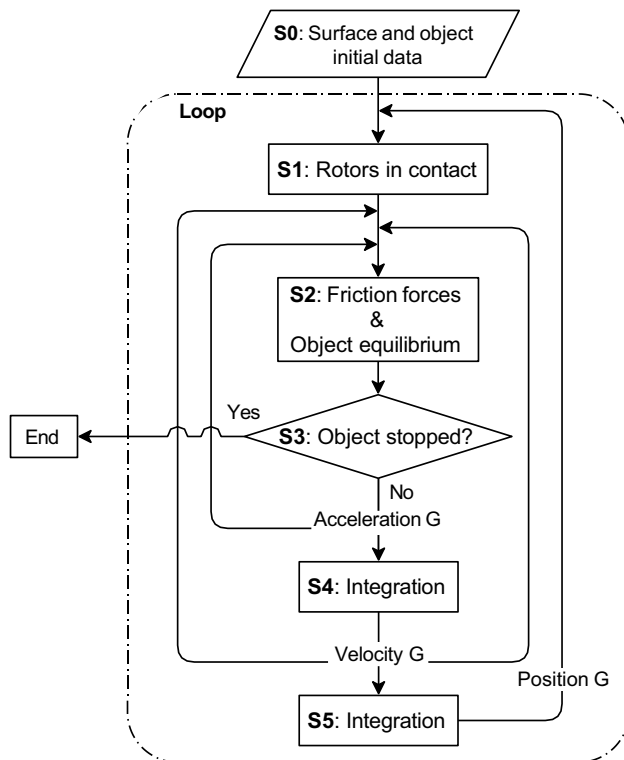
surface. If the motion is possible, the loop continues; otherwise, it stops;

S4. The acceleration, used to estimate the weight distribution on the contact modules, is then integrated to retrieve the object velocity;

S5. The velocity, after the check for the object motion and the application within the friction model, is also integrated to obtain the position.

The *Simulink* block diagram, incorporating these instructions and employed for the subsequent analysis and simulation, is illustrated in Fig. 3. The model consists of two main function blocks, i.e., **FB1** and **FB2**, some constant entries, i.e., *M*, *oc*, X_s, Y_s, *alpha*, z_g, *GD*, and *mu*, two integrator blocks, i.e., $\frac{1}{s}$, and two stopping units. In summary, the two function blocks observe the following logic:

Starting with **FB1**:

FB1.1 A preliminary check of the object presence over the surface is conducted exploiting the object position (x_g, y_g) and the rotors' arrangement (X_s, Y_s). If the part already reached the end of the simulation grid (containing both the modules and ball transfer units), the model stops. This assessment is introduced not primarily for functionality but to prevent *Simulink* errors;

FB1.2 With the geometrical (*GD*) and pose (x_g, y_g, t_g) inputs, the object contour is mathematically formulated;

FB1.3 The *inpolygon* function [35] is used to identify the points, among X_s, Y_s, that lie within or on the edges of a polygonal region described in FB1.2. The result is a grid-size matrix (*in*) of Booleans (0,1) marking with 1 the modules in contact with the object;

Instead, **FB2**:

FB2.1 The logic information of *in*, combined with the surface layout (X_s, Y_s), determines the positions of the contact points. Consequently, the velocities at these locations are computed using the speeds obtained from previous iterations (dx_g, dy_g, dt_g);

FB2.2 The rotor axes' orientation data (*oc*) are retrieved for each grid point;

FB2.3 The contact forces, normal to the surface, are computed using a minimization constrained function called *fmincon* [36], as the support is usually hyperstatic (object usually over more than 3 rotors). The function minimizes the norm of the vector containing these normal components, while ensuring adherence to the part's equations of equilibrium, which include translation along the *z* axis and rotation around the *x* and *y* axes. Furthermore, a constraint is imposed to ensure that the resulting forces remain non-negative, in line with physical principles;

Fig. 2 Flowchart of the iterative loop implemented in *Matlab* and *Simulink* to reproduce the object motion above the surface.
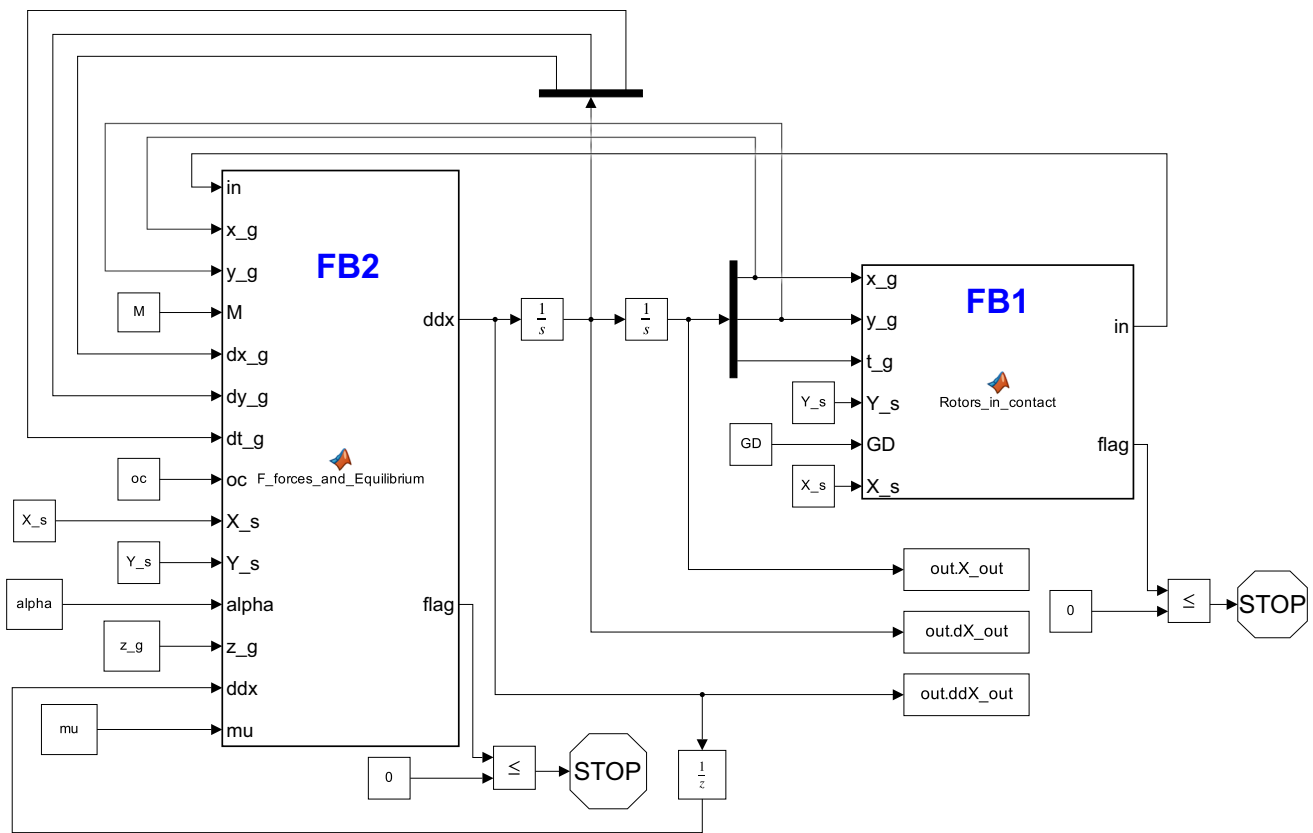
Fig. 3 *Simulink* block diagram used to simulate the object motion.

FB2.4 The analytic friction model is employed to assess the in-plane friction forces, i.e., F_{par} and F_{perp} (Section 2.1), acting on the rotors in contact. The object velocities (FB2.1), rotor axes' orientations (FB2.2), the normal components (FB2.3), and the friction coefficients (*mu*) are exploited by this model;

FB2.5 The main check about the object motion is done considering the velocity dx_g (along *x*, i.e., the direction of the line). If this speed is positive, the motion is guaranteed; otherwise, the inclination of the surface is taken into account. When the slope is steep enough to win, the total friction along *x* the motion proceeds, otherwise not.

FB2.6 The equilibrium of the body is computed and the acceleration vector (*ddx*) is retrieved and sent to the integrator to restart the cycle.

Therefore, overall, the correlation of the *Simulink* model with the steps' procedure (Fig. 2) is the following: **S0**, i.e., the initialization step, is done for *Simulink* with a main script assigning all the input data previously mentioned (above the steps list). **S1** is directly related to the function block **FB1**. This unit exploits the object pose (x_g, y_g, t_g) from the integrator, together with the object geometry (*GD*) and surface layout (X_s, Y_s) to retrieve the modules actually in contact with

the object. Conversely, **S2** translates into **FB2** in *Simulink*. In this case, the block receives as inputs the data concerning the surface arrangement (X_s, Y_s, *oc*, and *alpha* (*α*)), inertial and geometrical data of the object (*M* and z_p), and finally, the friction coefficients (*mu* (*μ*)). With these terms combined, all the friction forces acting on the part are determined, leading to computation of the body's equilibrium and the collection of acceleration terms (*ddx*). Similarly, **S3**, i.e., the moving condition check, is implemented in **FB1** too. Practically, the loop is stopped if the object reached a velocity along the line ≤ 0 m/s and the inclination is null or not enough to continue the sliding.

Finally, **S4** and **S5** simply take shape within the two integrators $\frac{1}{s}$ of Fig. 3 producing velocity and position from *ddx* to restart the loop.

3 Experimental setup

To assess the surface and its capabilities, the experimental setup is designed with a focus on three main potential applications: sorting, slowing, and stopping of material flows. Specifically, these activities are intended to evaluate the accuracy of the digital model mentioned in the previous

section. Each one of these applications serves to test the model in a different aspect: sorting involves complex trajectories away from the main line, while slowing and stopping evaluate the in-line motion (with its associated coefficients) and the halt condition, respectively. The following sections are going to introduce the resulting test bench, the design of the experiments, and the tests conducted.

3.1 Setup description

The setup assembled is meant to reproduce a sorting region along a transfer line for packages in the range of 1 to 10 kg (due to the prototype working constraints) and a flat base with a minimum footprint of 0.2 m × 0.2 m. It consists of an array of the concept *Modules* and *ball transfer units* mounted on a planar structure of 1.2 m × 0.7 m (Fig. 4). The modules are the copies of the prototype presented in Fig. 1(b) and are organized along the line direction in a 2 rows by 6 columns arrangement (yellow, blue, orange colored units in Fig. 4). On the other hand, the ball transfer units are *Alwayse®* 1006-14 nylon spheres and they are placed before and to the

side of the modules, respectively, as the *Starting position* of the box (Fig. 4) and as the area where the sorted box is sent (*Area after sorting* in Fig. 4). The main plane, where all these components are placed, is hinged on the one side and adjustable on the other (*Tilting Support* in Fig. 4) to control the inclination for the input motion. The available angles for the slope (α) are [7°, 8°, 9°, 10°]. The actuation of the modules' rotation axis is controlled by an *ARDUINO® Mega* board and 12 relay units. In this way, each rotor axis direction can be controlled (4 directions available) separately and exploited for other different tasks, while for the measurement of the object position during its motion, a *FLIR Blackfly® S* Monochrome Camera with 6.3 MP and 59.6 fps is used.

3.1.1 Camera calibration and uncertainty

The camera was calibrated with 31 pictures of a 10 × 14 chessboard (20 mm square side length) placed in all the areas of the field of view, at different altitudes and inclinations.

Fig. 4 Setup with its main components, areas, and coordinates
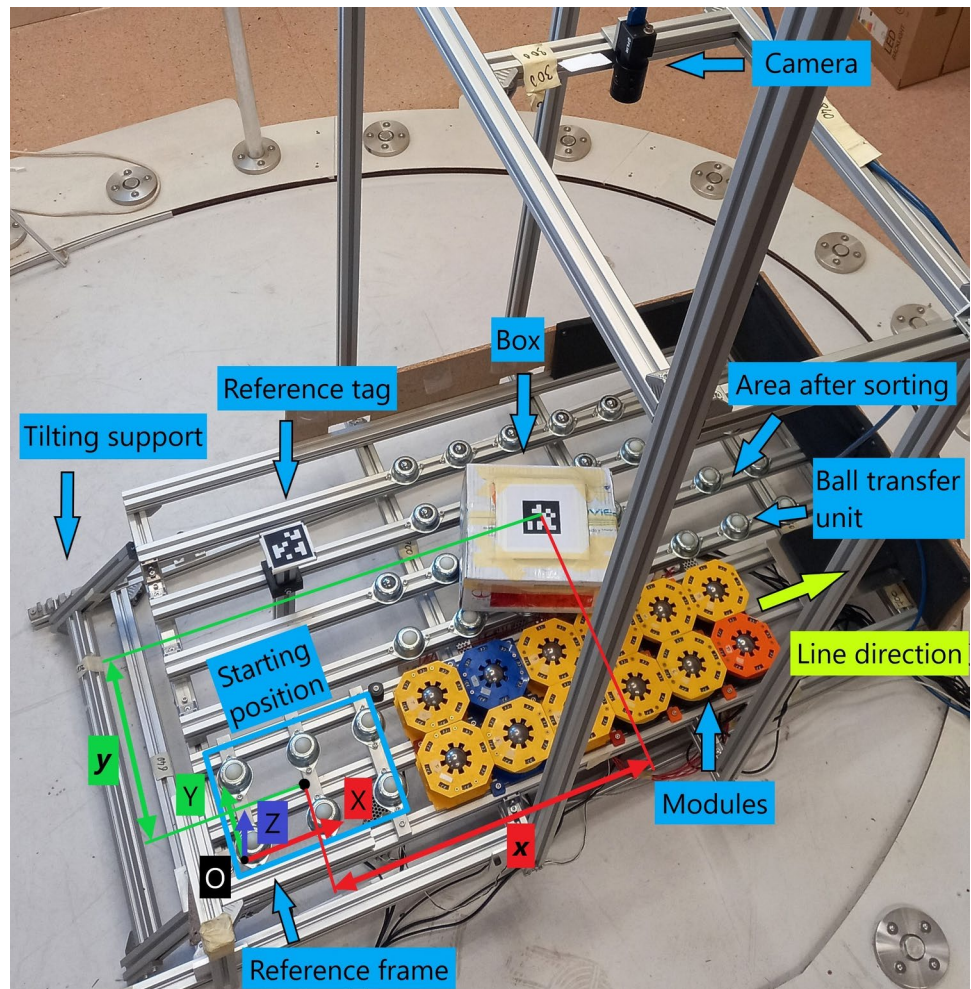
The resulting mean re-projections' error calculated by the Matlab built-in camera calibrator [37] was 0.23 pixels.

To increase the accuracy of the measurement, besides the thorough calibration of the camera, AprilTags were employed as fiducial markers [38] for the pose estimation of the surface (fixed — *Reference tag* of Fig. 4) and the box (mobile — *Box* of Fig. 4).

Eventually, the uncertainty of the camera measurement was studied to assess the quality of the visual system. The cases considered were two, a static measuring and a dynamic one. For both scenarios, a type B analysis (according to the GUM [39]) was conducted through Eq. (1) for *x* and *y* directions.

$$U = k \sqrt{\left(\frac{U_a}{k_a}\right)^2 + \frac{s_c^2}{n_c} + \frac{s_m^2}{n_m}} \qquad (1)$$

where:

- *U* is the expanded uncertainty.
- *k* is the coverage factor for the uncertainty according to the GUM [39], selected equal to 2.
- U_a is the expanded uncertainty of the calibration reference tags.
- k_a is the coverage factor for the uncertainty U_a according to the GUM [39] ($k_a = 2$).
- s_c is the standard deviation of the reference tags' distances measured in subsequent photos.
- n_c is the number of subsequent photos where the reference tags' distances are measured; 30 pictures were captured in each case.
- s_m is the standard deviation computed from the camera retrieved values during the measuring process.
- n_m is the number of repetitions of the measurement during the measuring process, which is equal to 1.

The setup built to evaluate the uncertainty of the camera measuring distances in *x* and *y* directions is presented in Figs. 5 and 6. Specifically, Fig. 5 shows the Apriltags reference grid, while Fig. 6 depicts the setup used for the dynamical evaluation of the uncertainty along *y* axis. The grid is 1080 mm × 720 mm, i.e., 7 × 5 tags, with tag sizes (side) of 60 mm (as the other Apriltags used in the measuring) and spaced by 180 mm. Additionally, the reference uncertainty U_a ($k_a = 2$), decomposed along the *x* and *y* axes, corresponds to the values listed in the first column of Table 1.

Moving on to the missing parameters of Eq. (1), their assessment is now introduced. To compute s_c, 30 pictures of the reference grid are captured in static conditions. Consequently, all the distances between reference Apriltags along *x* and *y* are measured for each image, i.e., 30 times each, resulting in a measurement distribution for every distance. Therefore, s_c, which is the standard deviation of these
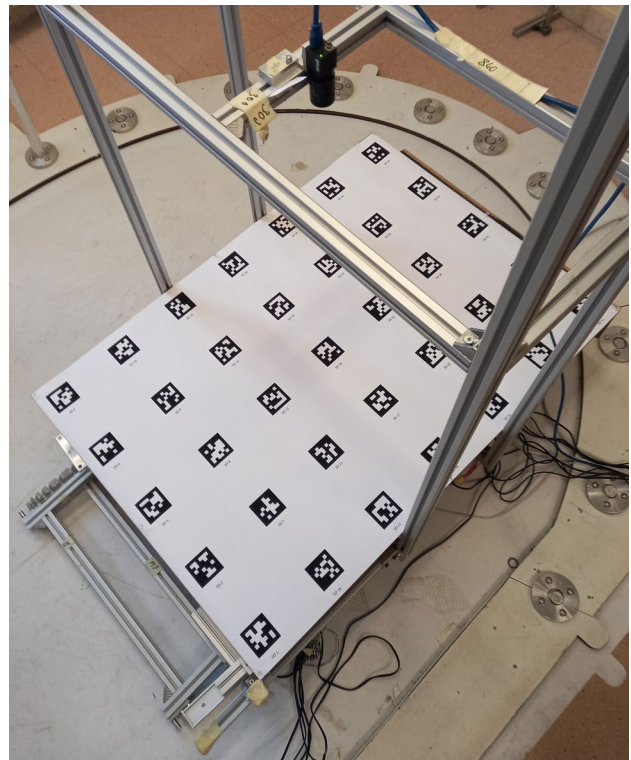

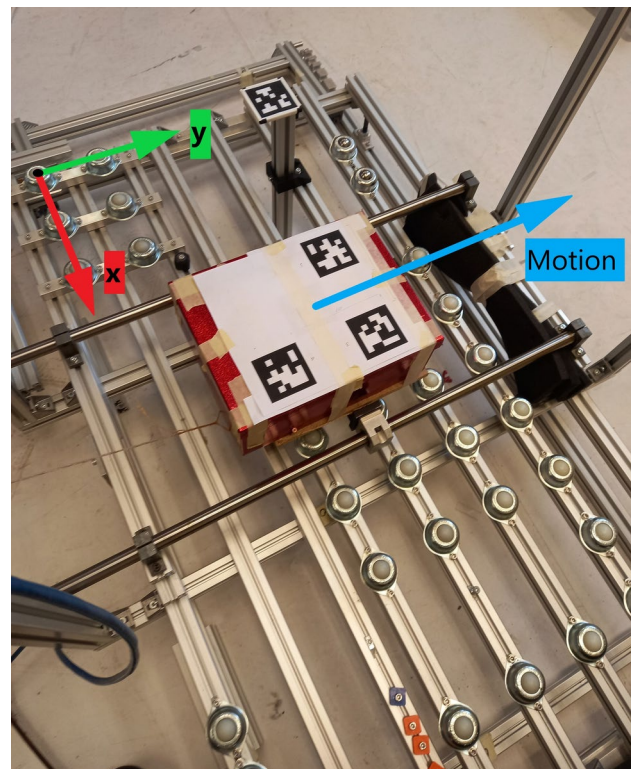**Fig. 5** Reference tags grid used to evaluate the uncertainty

Fig. 6 Guides and tags used for dynamic uncertainty evaluation along the *y* axis.

Table 1 Uncertainty terms along x, y for the static and dynamic cases

		Ua [mm]	sc [mm]	sm [mm]	U [mm]
X	Static	0.11	0.045	0.045	0.14
	Dynamic	0.11	0.045	0.67	1.34
Y	Static	0.12	0.049	0.049	0.16
	Dynamic	0.12	0.049	0.65	1.30

distributions, results in the worst case as in Table 1, differentiated by x and y directions.

Eventually, the last term connected to the measuring process, s_m, was the one different for the static and dynamic evaluation. Specifically, for the static case, the measurement process does not differ from the previous one of the reference grid tags; therefore, $s_m = s_c$ (Table 1).

On the contrary, for the dynamic evaluation, two linear guides and a slider were mounted on the surface along x and, as in Fig. 6, along y. Three Apriltags were placed on a box above the slider in order to conduct the distance measurement between the couple of tags x-aligned and y-aligned. Twenty trials and therefore 20 videos (in average 100 frames each) were recorded for each direction (x, y). With all these measurements, the standard deviations resulting from the distributions define s_m — "Dynamic" of Table 1.

Finally, with all these results together and Eq. (1), the overall uncertainty along x, y for the static and dynamic cases is summarized in the last column of Table 1. These values are assumed acceptable, according to the purpose of both the measurement and the physical system involved.

3.1.2 Measurement procedure

Moving on from the measurement capabilities, the setup operation can be introduced. Specifically, during the normal functioning of the test bench, the box, placed on the starting position in contact with the reference frame, is left free to slide towards the sorting/slowing or stopping modules, while the camera is recording the motion and Arduino is powering the rotor axes. The video of the box is then processed to extract all the data regarding its motion using Matlab. In practice, the Apriltag detection function (*readAprilTag*) is adopted.

3.2 Design of experiments

In a generic sorting operation, the primary outcomes are the completion time and the y distance from the starting position (Fig. 4), with orientation considered of secondary importance. The same is true for the stopping, but instead of y, the interest is about the motion along the line x. Lastly, for the slowing only matters the additional time produced.

All these outputs are affected by various parameters with complex inter-relations. Therefore, in order to gain a preliminary understanding of them and better plan the actual tests, the authors employed a Design of Experiment (DoE) with ANOVA approach.

Practically, the analysis was focused on the more complex application, i.e., sorting, and was conducted using the system's digital model of the setup. Because of this, the time constraint appeared less stringent; thus, a full factorial design with two levels was selected.

The parameters chosen as factors were as follows: μ_{max}, μ_{min}, μ_{out}, m, α, z_g, and B. The first two terms are the main friction coefficients describing the modules' functioning, and used in their analytic model (Section 2.1). The third term (μ_{out}) is the friction coefficient between the ball transfer units and the box, the fourth (m) is the mass of the box, followed by the inclination of the surface (α), the height (z_g) of the box center of mass (referred to the surface plane), and the base area (B). The high and low levels selected for these parameters are their average values estimated in [33] plus the errors that may be affecting their measurement. Specifically, a $\pm 10\%$ range was considered for the friction coefficients and z_g, a $\pm 5\%$ for B, and a $\pm 2\%$ for α and m.

Eventually, the results of the ANOVA analysis conducted on the average values of Table 2 are summarized in the Pareto chart of the effect size of Fig. 7. The two outputs reported are those considered of greatest importance for sorting, i.e., the sorting *Time* and the final distance moving away perpendicularly from the transfer line (y). These values are collected fixing the final x displacement. However, if the simulation time were fixed and the x displacement served as the output, the finding would have been equivalent (as *Time* in Fig. 7). The graph shows only the first ten parameters, and their combination, with the highest effect size. Despite this, the only ones truly relevant are those with the cumulative outcome above 5% (dotted lines in Fig. 7).

The most relevant terms are the two main friction coefficients describing the module (μ_{max}, μ_{min}), the one of the transfer units (μ_{out}), and the inclination of the surface (α). This outcome points out that, for a good prediction of the surface with the digital model, these input factors have to be sufficiently accurate. On this context, the tilting angle is not problematic, as it does not change with the objects transported and is quite easy to assess, even with higher

Table 2 Average factors values used for the DoE and ANOVA study

μ_{max}	μ_{min}	μ_{out}	m [kg]	α [°]	z_g [m]	B [m × m]
0.2	0.07	0.04	7.5	10	0.04	0.245 × 0.215

Fig. 7 Pareto charts of the standardized effect size of the *Time* taken and the *y* displacements for a fixed *x* displacement
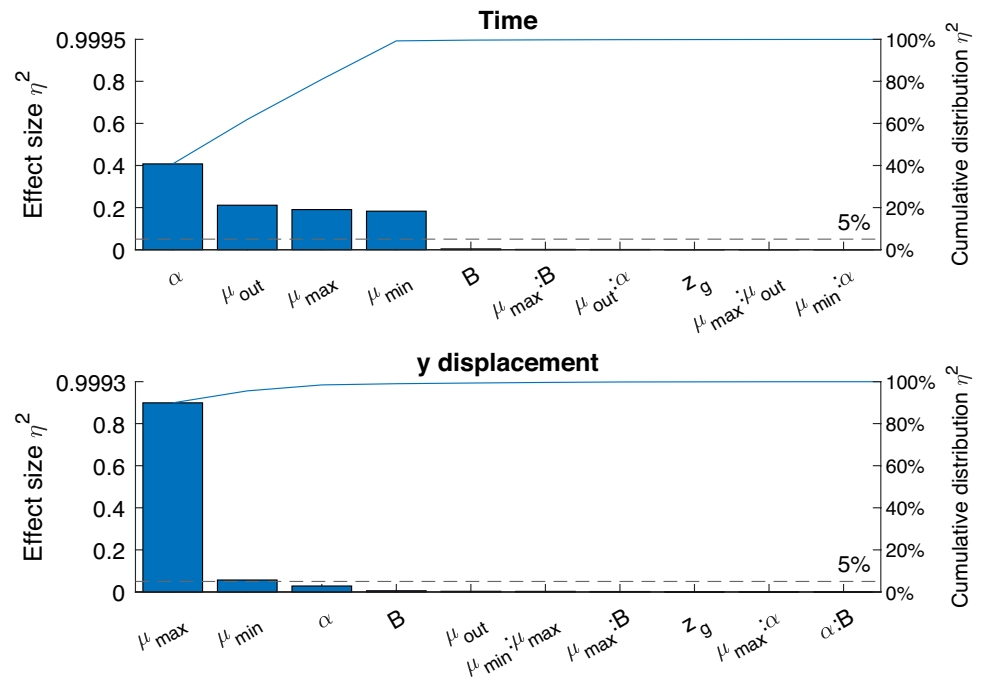
precision. On the other hand, the friction coefficients are connected to many factors, such as the materials in contact and the roughness of their surfaces, just to name two. This brings a difficulty for the surface predictions because different kinds of packages and materials can have a perceivable difference in terms of friction coefficients. However, usually, the transport lines work with standard materials, e.g., cardboard boxes, plastic, and wooden containers; thus, once their data are determined, predictions can be made. On this subject, in Section 3.3 is presented an optimization technique that permits to adjust the digital model on the current material and compute the specific friction coefficients. Moreover, in other circumstances, if the surface is used with a feedback control, e.g., real-time position from a camera, the errors can be corrected and the real coefficients determined step by step (dynamic parameters regressor).

3.3 Tests

As a result, the tests planned for the setup dedicated to three main tasks, i.e., sorting, slowing, and stopping, involve variations in the following: box type (cardboard shipping package: Box type A, PVC covered cardboard box: Box type B), surface inclination ($\alpha_1 = 7°$, $\alpha_2 = 8°$, $\alpha_3 = 9°$, $\alpha_4 = 10°$), and box mass ($m_1 = 4.7$ kg, $m_2 = 7.5$ kg). The first two parameters are outcomes of the DoE analysis, as the alteration of the box type is prompted by the challenge of pre-selecting friction coefficients, while the inclination was directly a prominent output-affecting factor. On the contrary, the mass did not emerge among the DoE impactful parameters. However, as previous studies have highlighted (according

to [33] and components catalogs), weights affect friction coefficients for diverse reasons (mainly μ_{min} and μ_{out}). An example is the contact area deformation, amplified by the mass and the reduced stiffness of materials like cardboard or plastic. Another one is the load that the bearing spheres require for rolling smoothly or more efficiently. Therefore, in summary, also the mass is modified during the experiments, not as direct outcome of the DoE, but as cause of variations on the friction, which is the actual DoE prominent output.

In addition to the variations presented (α, m, Box *type*), the different operations planned (sorting, slowing, stopping) require also specific orientations for the rotor axes of the controlled modules. To simplify the tests for the sorting and stopping analysis, all the modules were actuated in the same way. Specifically, for the sorting, the totality of the modules was with the axes oriented at 135° (anti-clockwise) with respect to x axis (Fig. 8), while for the stopping, the orientations were all of 0° with respect to x axis (as the fourth red row of Fig. 9). Activating equally all the modules in this condition was possible given the fact that was not important to limit the output. In other words, for the sorting the objective was the package out of the line no matter the x, as for the stopping the important thing was just the halt along the line. On the other hand, the slowing was evaluated trying to have 20% increase of time; therefore, only few rows of modules had to be actuated (against the motion) and were not obvious in advance which ones. The orientations of these axes were 0°, as for the stopping, while the rest of the modules were at 90° like in Fig. 9. However, depending on the inclinations, mass, and box type, the number and the position of the actuated modules were different.
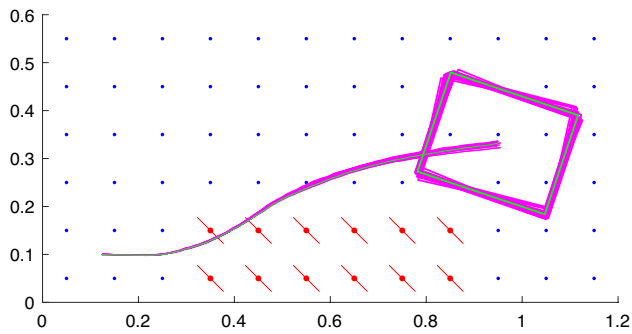
Fig. 8 Trajectories of 15 measures (magenta) and their median (green) during a sorting task, with $\alpha = 8°$, $m = 7.5$ kg, and Box *B*
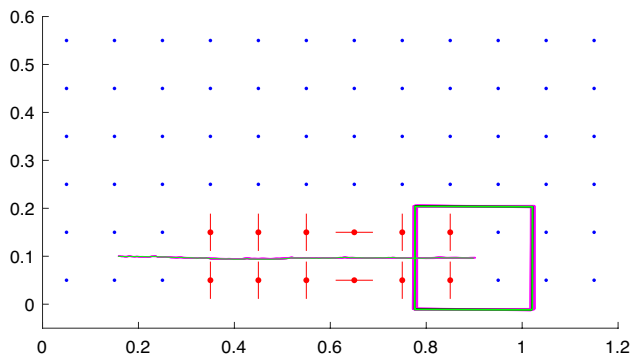

Fig. 9 Trajectories of 15 measures (magenta) and their median (green) during a slowing task, with $\alpha = 8°$, $m = 7.5$ kg, and Box *B*

For each combination of material, mass, and inclination, 20 measurements are conducted. Out of the 20 evaluations, 15 are used to determine the median, employed as reference trajectory, while the remaining 5 are employed to assess the error made by the digital model prediction. An example of these 15 measures and their median is reported in Fig. 8 for the sorting, and in Fig. 9 for the slowing. In these pictures, the magenta lines and rectangles represent respectively the trajectory and final position of the box base measured with the camera during the 15 trials and reported on *Matlab*, while the green lines are the corresponding medians and thus the benchmark path.

Regarding this matter, Fig. 10 summarizes the connection between the digital and the real layouts and results. Specifically, the image illustrates the overlapping of the two arrangements, with the red lines describing the direction of the rotor axes selected (for the sorting) and all the points indicating the centers of the modules (red) and ball transfer units (blue). Moreover, also the box is visible, showing that the digital version is over the base of the material one, as should be. Lastly, this match between the real motion and the virtual environment permits to count automatically the number of modules in contact under the box along the trajectory. In detail, Fig. 10 depicts this trend with a black

continuous line and the number of modules with dotted lines. On this point, the experiments conducted show that the center of mass of the box follows a generally smooth trajectory despite passing over different modules (black lines in Fig. 10). This occurs because the transition is gradual with only minor impacts. In fact, the influence of having more or fewer modules beneath the package primarily affects orientation, while displacement appears only as a secondary and gradual effect. To be more specific, a new module oriented even differently has a relevancy on the resultant force of about 1 divided by the number of rotors, and therefore, it is limited. On the other hand, the torques differ more because they also involve the moment arms. Consequently, only once both the rotational effect and the resultant variation become significant, they can gradually impact the displacement.

Moving back to the testing, the reference trajectory is used to establish for every case the input values for the parameters in the simulations. Among these inputs, not all of them are straightforward. In particular, the challenge arises with friction coefficients, as they cannot be pre-selected, and because of their variability influenced by several parameters, e.g., roughness and materials. In general, for few specific experiments, these terms can be measured and it is not a major problem, but it may be in an industrial application, e.g., if a new batch of plastic containers is bought by the company to transport its parts. Therefore, to give a flexible and faster solution, the authors proposed to adopt an optimization algorithm to calculate them (μ_{max}, μ_{min}, μ_{out}). For this experimental setup, the Matlab *lsqnonlin* [40] algorithm was used. Specifically, the objective function to minimize was the difference between the real and the simulated final position and times of the sorted/slowed or stopped object. Once the coefficients are settled, together with the other inputs (α, m, and all the others), simulations are ready to be launched and their outcomes compared to the five experimental results to assess the errors and consequently the accuracy of the digital model prediction.

4 Results

The tests have been concluded, allowing for the presentation and analysis of results. In this regard, we will describe in Section 4.1 the means and standard deviations of the output parameters obtained from the 20 measurements for each task: sorting, slowing, and stopping. Furthermore, the discussion will encompass the examination of all the distinct input conditions (α, m, Box *type*). Secondly, in Section 4.2, the prediction accuracy evaluation will be presented. Here, the relative percentage errors between the digital model and the experimental outcomes will be unveiled. Finally, in Section 4.3, the subject is going to be an additional analysis about the system performance.
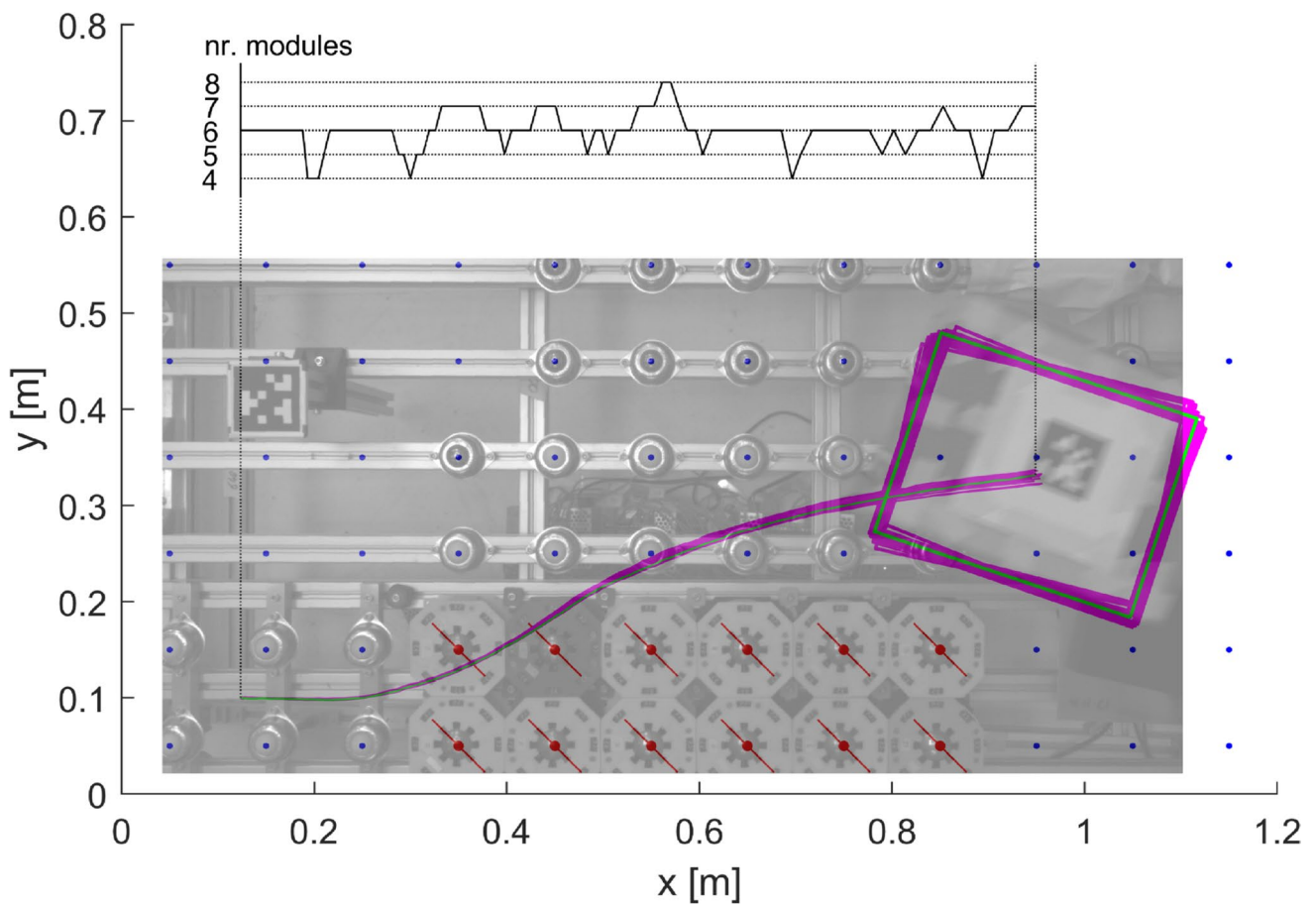
Fig. 10 Frame of the video used for the measurement and *Matlab* arrangement overlapped to show the layout and the markers meaning; the magenta line shows the real object trajectory, while the black one represents the number of modules (*nr. modules*) in contact with the box along the same trajectory

4.1 Measurement outcomes

Starting from the sorting, the relevant outcomes are the sorting *Time* and the final *y* displacement (fixing the final *x* displacement). These are reported in Fig. 11. Here, the error bars of the standard deviations show limited variability for each set of measurement, serving as a quality check for the setup and also supporting the following reference trajectories identification. The main causes for the slight variabilities have been traced back to minimal (< 1 mm) misalignments of the modules and transfer units *z* positioning, and, above all, to the rigidity of the box. Precisely, they both cause impacts between the box and the surface contact points during the motion. In fact, because of the misalignment, the contact points are not on the same plain. Additionally, due to the low stiffness of boxes, the deformation of the packages on the rotors is decreasing the height of the contact plane below the top of the spheres. Summing up these two characteristics, the impacts that may occur when a box encounter a new rotor are evident, especially when the

velocity of the object is modest. The stiffness consideration is also supported by the wider error bars obtained for the less rigid box, i.e., Box *A*.

On the other end, the mean bars highlight the influences of the parameters on the outputs, confirming the predictions of the DoE. Specifically, the descendent trend in the time subplot evidences the inclination α impact, i.e., the bigger α the quickest the sorting (same *y* reached), while the different lengths of the bars related to the two box types mark the consequences of diverse friction coefficients. On the same line, also the mass results moderately influential, as there are minor discrepancies between the bars of the same type and inclinations, but different weights. Particularly, the most evident impact of mass on the friction is for the less rigid Box (*A*), according to the reason previously mentioned.

Additionally, with respect to the *y* displacements in the second subplot, two threshold lines are also highlighted. These dashed lines illustrate the *y* values for each box type when the displacement of their respective center of mass is 75% of the box semidiagonal away from the sorting line,

Fig. 11 *Time* and *y* displacement mean outcomes (bar plots) with their standard deviations (error bars), and the sorting limits (dashed lines)
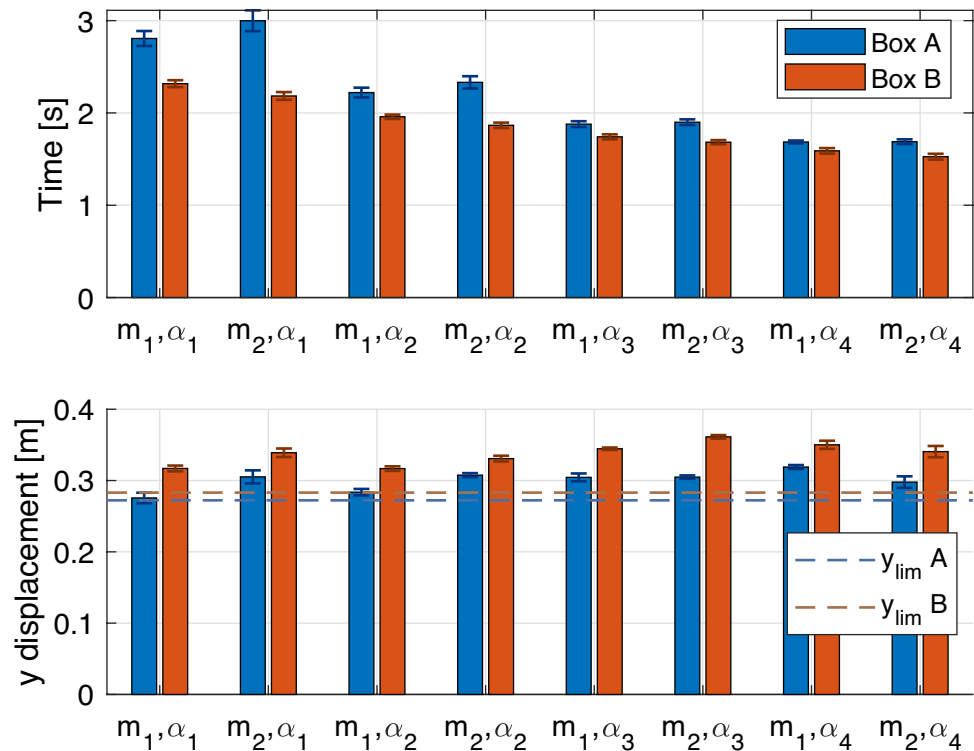
i.e., $y_{lim} = y_{maxL} + 0.75D/2$, where y_{maxL} is the y coordinate of the second row of sorting modules and D is the diagonal of the box base. This condition is assumed as average status of achieved sorting despite the orientation and looking at the plot (Fig. 11) is fulfilled in all scenarios, verifying the concept capabilities.

Continuing with the analysis of slowing and stopping, Figs. 12 and 13 present the main outcomes of these tasks. Respectively, for the slowing, the outputs are the *Time* spent during the operation (top subplot Fig. 12) and the ratio (bottom subplot Fig. 12) of this time with the one resulting from the same path, but with the rotors oriented to assist the descent (*Time$_{free}$*), while, for the stopping, the outcomes are the *Time* (top subplot Fig. 13) to arrest the movement and the final x displacement along the line (bottom subplot Fig. 13). For both operations, the error bars show limited variability, even though slightly higher than for the sorting, especially for the time outputs, because of the lower speeds and the higher influence of impacts during the deceleration. Instead, the mean bars highlight the influence of the controlled parameters over the motion. Specifically, considering the slowing, as the inclination increases (from α_1 to α_4), the overall time is reduced, although the time ratio is the same. Moreover, Fig. 12 (bottom subplot) shows that the minimum 20% increase of motion time is achievable for all the input parameters, except with the combination m_1, α_1, Box *A*. This outlier is due to the prototype surface limitations, i.e., layout and number of modules available for the task. However, more importantly, it highlights again the effect of the mass,

which, other parameters being equal, in one case makes the motion possible and in the other not.

Similarly, the stopping mean bars also reflect the inclination variation. Practically, the x displacement rises with α requiring approximately always the same time. In Fig. 13 (bottom subplot), the x distances of the stopping modules' columns are reported with dotted lines. As visible, the steeper are the slopes, the further ahead columns are reached, up until the center of mass overcomes the second column of modules (the front of the box is preceding on the third column). Also for this task, the mass has a moderately evident effect, the same applies to the box type for both slowing and stopping.

Eventually, the three figures (Figs. 11, 12, and 13) summarize the measures retrieved from the setup for the different tasks, showing the capability to complete them, the effect of the main inputs, and the little variation during the measurement process.

To conclude, as an additional comment to what has already been highlighted by the tests, a more general consideration can be made. In practice, although these tests were conducted under standard operating conditions, the system's design suggests the potential to handle more complex scenarios that may occur in practice. Common issues affecting material handling and transportation systems of this kind include random orientations of packages, misalignments, or excessive proximity between them. These challenges are typically addressed by basic conveyors using filters, barriers, or other additional components,

Fig. 12 Slowing *Time* and *Time ratio* mean outcomes (bar plots) with their standard deviations (error bars), compared with the condition without slowing (dotted line) and the one requiring 20% extra time (dashed line)
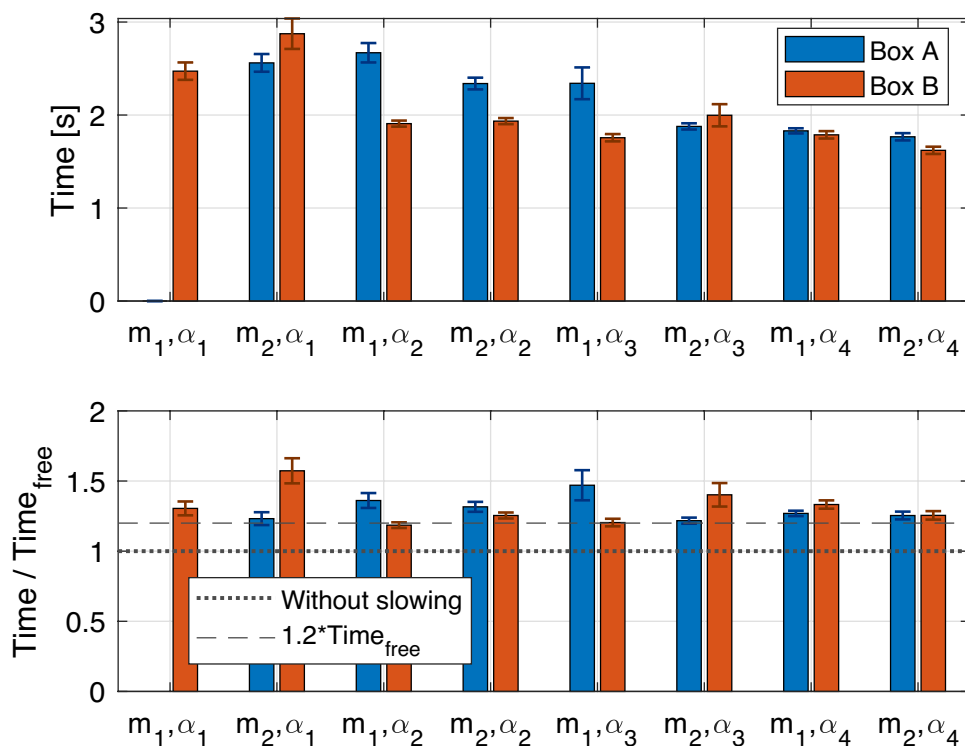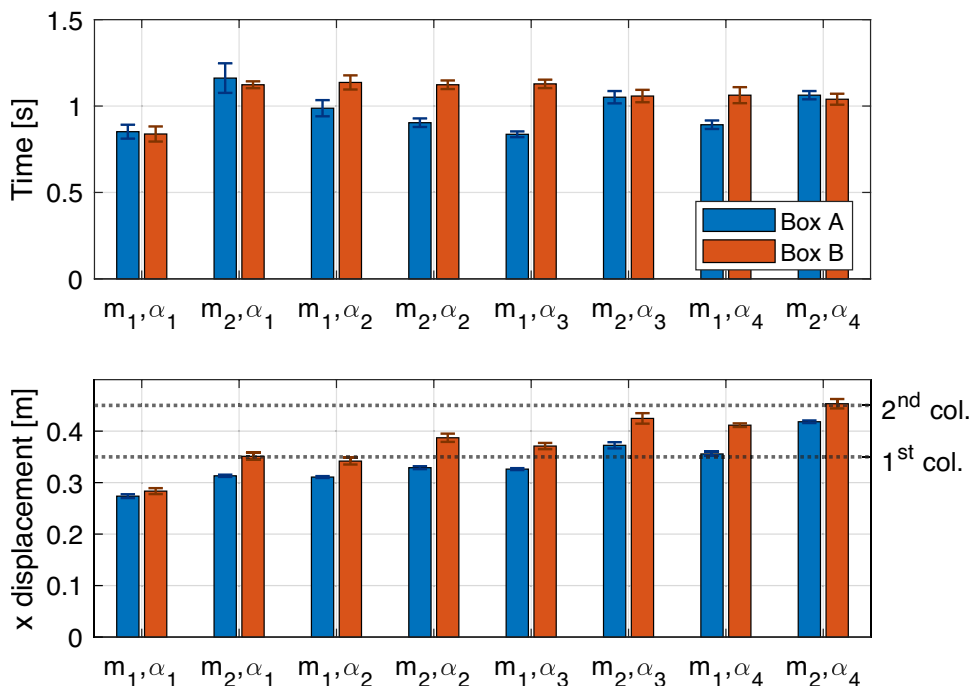
Fig. 13 Stopping *Time* and *x* displacement mean outcomes (bar plots) with their standard deviations (error bars), and *x* coordinate of the stopping modules columns (dotted lines) encountered by the center of mass.

whereas intelligent systems also incorporate control mechanisms ([2]). The system developed in this article is meant to adopt this latter approach, as each module can be potentially controlled independently, and with the use of a camera, constant feedback on the material flow status is possible. In practice, solutions to problematic conditions can be envisioned by combining the movements tested in this section. For example, if two stacked packages arrive on the line, slowing down the rear package would create distance, allowing the task to be completed. Similar strategies are also adopted by other motorized intelligent systems, adapting to their design and, most importantly, to the specific problem.

4.2 Prediction accuracy

As explained in Section 3.3, every set of 20 measurements was split into a reference (15 trials) and a control sample (5 trials). Then, for each input combination (m, α, Box *type*), the median of the reference samples was exploited by the minimization algorithm to retrieve the optimized friction coefficients that produce the closest outputs. Consequently, the results of the optimized coefficients became the reference values for the digital model. At this point, for each input condition, the control sample was compared with these simulated counterparts, evaluating their goodness. Figures 14, 15, and 16 present the relative percentage errors resulting from this assessment employing a boxplot for each combination of initial values (m, α, Box *type*). Respectively, the three figures report these errors for the most important outcomes of each task, i.e., x, y, and *Time* for sorting, while exclusively x and *Time* for slowing and stopping. Additionally, in the graphs,

the overall maximum coefficients of variation (σ^*) of the measurements are displayed using dotted lines.

Starting from the sorting outcomes, the differences with the simulation for both displacements (x, y) and *Time* are very limited, on average below 1.2%, 5%, and 4% respectively. In addition, to confirm the goodness of the digital model prediction, the figure reveals that the errors for the y displacement and the *Time* are respectively below $3\sigma_y^*$ and $3\sigma_t^*$. Therefore, the prediction error is comparable or minor to the corresponding measurement variability. For the x error, the case was different since the experimental final (x) displacement was used as cutoff condition for the real data recording. Hence, its coefficient of variation (σ_x^*) is related to the frame rate of the camera and consequently smaller than for y, and *time*. However, despite this, $3\sigma_x^*$ is still comparable with the x error confirming the prediction quality.

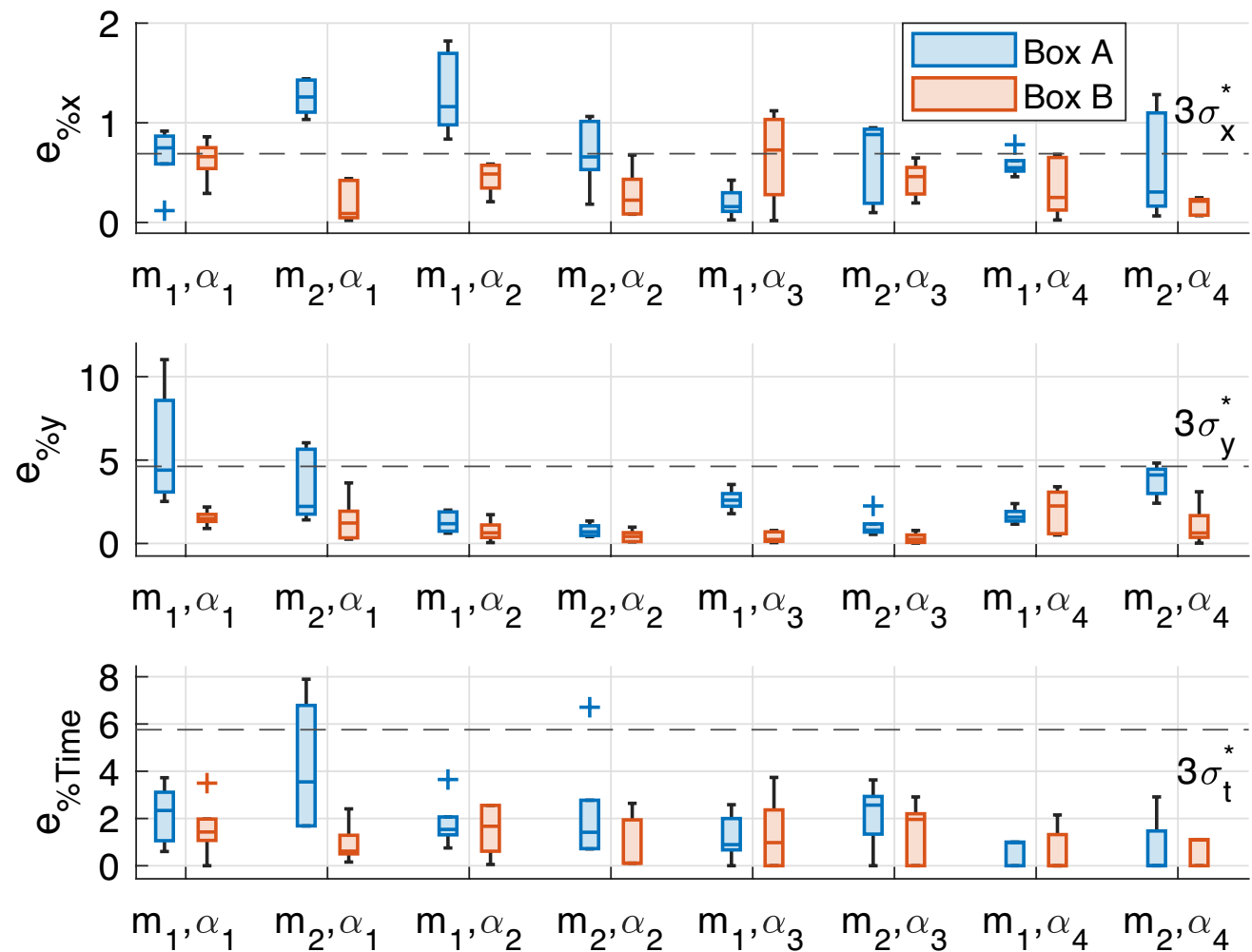Moving on to the slowing and stopping results, the boxplots reported in Figs. 15 and 16 concern exclusively the x

Fig. 14 Sorting errors (boxplots) of x, y, and *time*, between the control sets and the simulation results with their coefficients of variation (dotted lines)

Fig. 15 Slowing errors (box-plots) of x and *Time*, between the control sets and the simulation results with their coefficients of variation (dotted lines)
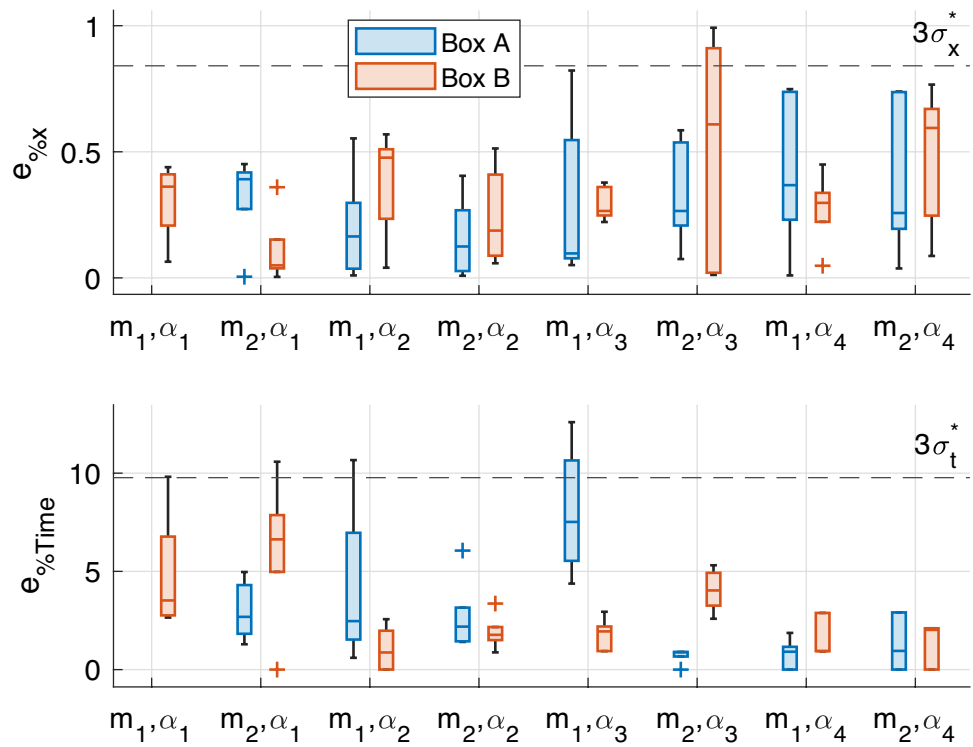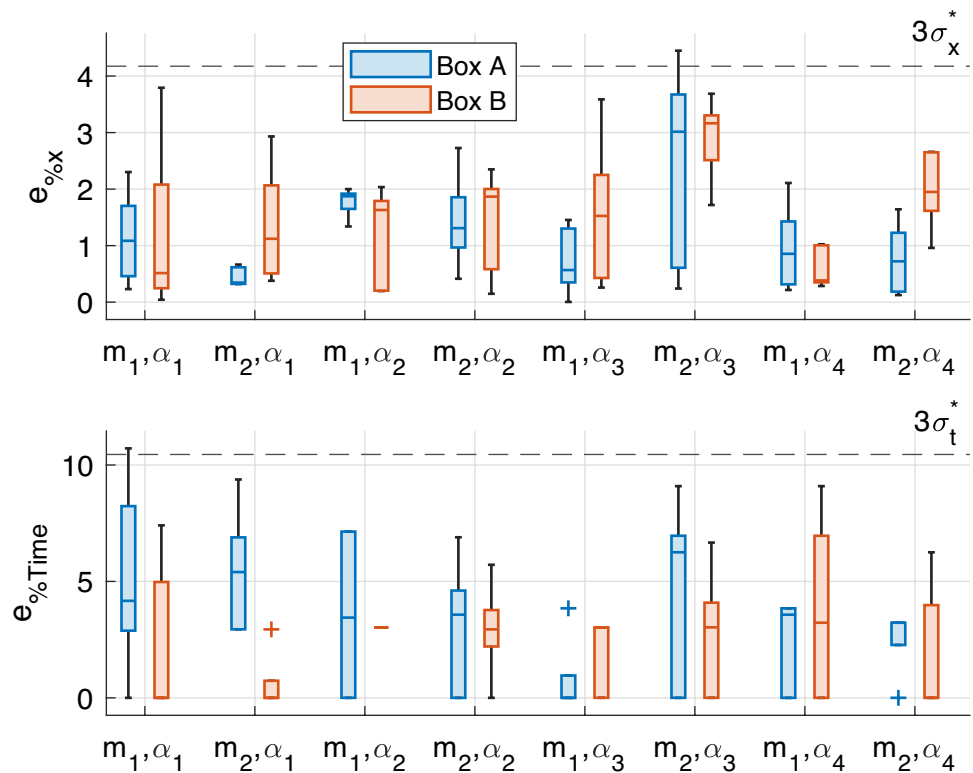

Fig. 16 Stopping errors (box-plots) of x and *Time*, between the control sets and the simulation results with their coefficients of variation (dotted lines)

displacement and the *Time*. In fact, for these two tasks, the object is not moving away from the line (x), but alters only its velocity. Both figures present high-quality predictions, specifically the relative percentage errors of x, i.e., $e_{\%x}$ are on average under 0.6% and 3% respectively, while, the *Time* ones are mean-wise under 7% and 6%.

Additionally, also in these cases, the errors appear below the respective coefficients of variation, leading the authors

to believe that the digital model is satisfactorily accurate. Similarly to the sorting, the *x* displacement, for the slowing task, was a cutoff condition for the recording; therefore, the same explanation for σ_x^* is applicable.

Contrarily, for the stopping outcomes, because of their intrinsic ending process, σ_x^* was directly related to the measurement variability.

The friction coefficients, derived from the minimization procedure which returned the boxplots in Figs. 14, 15 and 16, are summarized in Fig. 17. Each boxchart in Fig. 17 refers to a friction coefficient, i.e., μ_{out}, μ_{min} and μ_{max} and a box type, *A* and *B*. The outcome values indicate an overall higher μ_{max} and minor μ_{min}, μ_{out} for the Box *B* compared to Box *A*. This is imputable to the higher friction between the two materials (visible from the μ_{max} outcome), but also to the rigidity of the box.

In fact, the less rigid Box *A* deforms more on the rotors worsening the sphere spinning and increasing the impacts effect every new module is encountered during the box motion. These conditions, with the modeling through friction coefficients, result in greater μ_{min} and μ_{out} overall values for Box *A*. Additionally, the rigidity together with the box weight and the inclination appears to produce different coefficients for the same box type (whiskers and quartiles lengths of the boxplots in Fig. 17). The reason is always connected to the impacts, which are greater with higher deformation, i.e., with increased mass, and more significant in case of lower inclinations (α). As a conclusion, the friction coefficients retrieved from the algorithm appear to be in line with the working principle (Section 2.1) and with the values employed for the DoE. In fact, respectively, the condition of higher μ_{max} and minor μ_{min} was satisfied. Furthermore, the magnitudes are similar to the ones measured with the

setup introduced in [33] (cardboard-steel contact) and implemented within the DoE.

4.3 Performance analysis

Given the promising prediction accuracy results, the simulation environment was employed to evaluate the system's sorting capacity across wider input ranges. Sorting was selected again as subject of this investigation, as appears to be one of the most relevant tasks of intralogistic operations. Because of that, in fact, some comparison terms could be found in the literature [41] and could be employed as reference for the study.

Before presenting the input data and the performance results, some general considerations and comparison with current existing technologies can be done. As introduced in Section 3.1, the concept is capable of working with objects with at least one flat surface, covering at minimum four modules, i.e., a footprint of 0.2 m × 0.2 m (one module is 0.1 m × 0.1 m). On the other hand, there are no limits on the maximum dimensions of the parcels if enough modules are available to create that surface. On this subject, and considering the prototyping stage, the characteristics are totally in line with current systems, just to mention two relevant references: the sorting disks from [41] (well-established sorting technology), or the commercial smart surface, *Celluveyor* (novel, but already widely employed technology) [2]. Specifically, these two work with the same flat-faced objects, of which their very minimum footprint accepted is 0.15 m × 0.15 m (according to [41] and *Celluveyor* catalog). The shape of the flat base is not important for the solution proposed in this paper nor for the existing systems. The concept load capacity, instead, appears even higher than the existing sorting disks ([41]) and exactly the same 200 kg/m^2 as the *Celluveyor* in its 0.2 m modular version. Additionally, considering the technology employed by the authors' rotor, this limit is only to guarantee the perfect functioning in this prototyping stage; in fact, being a transfer unit with a sphere diameter of 40 mm, the resistance load could be around 100 kg/module (according to the lightweight solution in [42]). Considering this, even with overloads, the device is capable to work.

The analysis was conducted considering the two boxes of the experiments as reference. Alongside, the line's sorting space, matching similar systems (sorting disks according to [41]), was set at 1.3 m, with the same setup layout. The sorting rate is defined using pieces per hour (pcs/h) as follows: 3600/*ts*, where *ts* is the time (in seconds) that the package needs from the beginning of the 1.3 m to reach y_{lim} condition. Both boxes had a 7.5 kg mass, and as friction coefficients: [μ_{max} = 0.203, μ_{min} = 0.097, μ_{out} = 0.078] for Box *A* and [μ_{max} = 0.211, μ_{min} = 0.094, μ_{out} = 0.054] for Box *B*. These values resulted from the same minimization
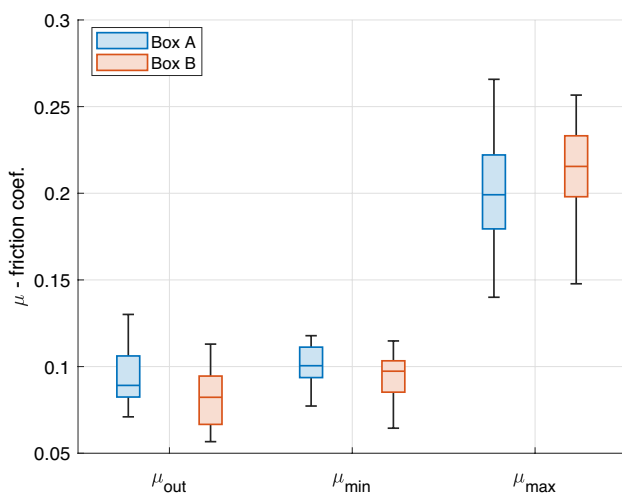

Fig. 17 Boxplots including all the friction coefficients μ_{out}, μ_{min}, and μ_{max} resulting from the minimization algorithm applied in the simulation of the three tasks (sorting, slowing, and stopping)

technique, but counting all cases (m, α) together for each box type. This approach ensures total reference coefficients independently of mass and inclination, making them preferable for studying the effects of inputs even outside the tested ranges.

For these new frictional terms, the errors evaluated with the control samples were slightly higher, i.e., under 10% and 15% for x and y displacements and under 4% for the time. Figure 18 reports the performance analysis results. The input conditions tested were the inclinations in the range $\alpha = [5°–14°]$ (blue markers), the initial velocities in the range $V_0 = [0.8 \text{ m/s}–2.8 \text{ m/s}]$ (red markers) and their combination, on the one hand the same α range plus also a constant $V_0 = 0.5$ m/s (cyan markers), while on the other hand, the V_0 range plus a fixed $\alpha = 5°$ (black markers).

From Fig. 18, the effects of V_0 and α on the sorting rate appear the following: α yields lower sorting rates (blue markers), which can be enhanced by adding V_0 (cyan markers), e.g., with longer input ramps before the sorting modules. The velocity instead performs better in terms of sorting capability (red dots), but has a tighter range of initial values available. However, these limits can be expanded combining this motion source with the inclination (black markers). Additionally, the figure shows the effect of friction coefficients and their ratios. Precisely, comparing μ_{max} and μ_{min} for Box A (∗ markers) to those of Box B (° markers), it is observed that the higher friction ratio μ_{max}/μ_{min} of Box B significantly enhances the sorting capability.

Finally, the sorting rates achieved for both Box types fall within the medium sorting capacity range [41] for nearly all input scenarios. Moreover, there is a margin for improvement by exploring alternative V_0 and α combinations, along with the adjustment of the friction ratio μ_{max}/μ_{min}, which can be optimized in a second prototyping stage. This conclusion
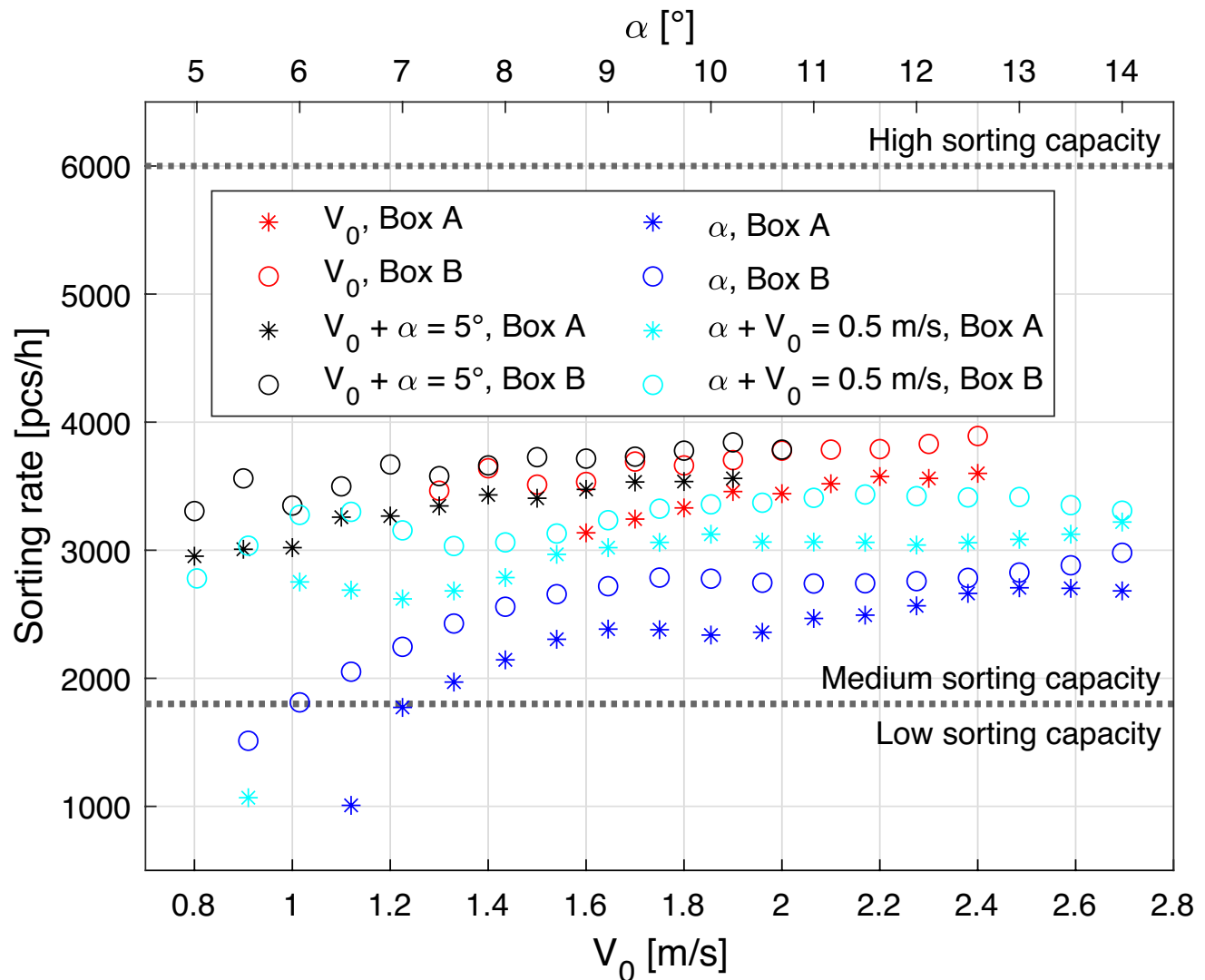

Fig. 18 Sorting rate with different input conditions: V_0, α, and Box types

demonstrates the effectiveness of the surface for its intended purpose, as its capability is equivalent to the one of the systems within the same class and the majority of other commonly used sorting technologies reported in [41]. Additionally, also the flexibility and versatility of the digital model are confirmed by its capabilities to test wider ranges of input conditions.

Summarizing the findings introduced in this section, the proposed concept shares the same operational ranges and constraints (footprint, weight, and the flatness of the object's base) as the currently used systems (*Celluveyor* and sorting disks as references). Similarly, according to this analysis, its performance aligns with current technology standards. Remarkably, these results are achieved despite the concept's simplified design, which requires no motors, while the *Celluveyor* and sorting disk systems require 3 fixed motorized wheels in the former case and 1 motor for swiveling and 1 or more for wheel spinning in the latter. As a result, the components in the paper's solution are simpler (spheres, coils, and pins, compared to motors, axes, omnidirectional wheels, transmissions, etc.) and require lower maintenance. Moreover, actuation control is minimal (on/off for a pair of coils), as is power consumption, which is limited to axis definition and relies on gravity and/or the object's previous velocity for active driving.

5 Conclusion

The smart surface introduced in this paper emerges as a novel sorting and feeding system for material handling inside factories and warehouses. The prototype presented and used for testing the concept achieved performances within the medium sorting capacity range, with rates up to 4000 pcs/h and margin for improvement. Similar results are in line with the current technologies implemented in industry, but with the main advantages of being accomplished by a more essential design and avoiding motors. In fact, the system proposed is underactuated; hence, it exploits gravity, objects previous speed, or both to achieve its tasks, aiming to reduce costs and energy consumption. The experiments carried out demonstrated the capabilities of the device for three main tasks of material handling, i.e., sorting, slowing, and stopping of packages. Additionally, they highlighted the effects of the input parameters and condition that can affect the surface operation. The study was accompanied by the evaluation of the system's digital model proving, given the very limited prediction errors, its accuracy, and justifying its use for industrial purposes. Finally, on top of that, a method, applicable also in industrial environments, to determine the essential parameters for the surface prediction is proposed, increasing the concept flexibility and adaptability. Moreover, the model adjusts to changes in transported parts, broadening the system's application to a wider range of parcels and scenarios beyond those outlined in the paper.

Declarations

Competing interests The authors declare no competing interests.

References

1. Fantoni G, Santochi M, Dini G, Tracht K, Scholz-Reiter B, Fleischer J, Kristoffer Lien T, Seliger G, Reinhart G, Franke J, Nørgaard Hansen H, Verl A (2014) Grasping devices and methods in automated production processes. CIRP Ann 63(2):679–701. https://doi.org/10.1016/j.cirp.2014.05.006
2. Uriarte, C., Asphandiar, A., Thamer, H., Thamer, H., Benggolo, A.Y., Freitag, M.: Control strategies for small-scaled conveyor modules enabling highly flexible material flow systems. ScienceDirect, Procedia CIRP Conference on Intelligent Computation in Manufacturing Engineering, 18-20 July 2018, Gulf of Naples, Italy (2018) DOI: https://doi.org/10.1016/j.procir.2019.02.117
3. Boutoustous, K., Laurent, G.J., Dedu, E., Matignon, L., Bourgeois, J., Le-Fort-Piat, N.: Distributed Control Architecture for Smart Surfaces. In: The 2010 IEEE/RSJ International Conference on Intelligent Robots and Systems October 18-22, 2010, Taipei, Taiwan (2010). DOI: https://doi.org/10.1109/IROS.2010.5650668
4. Dang TAT, Bosch-Mauchand M, Arora N, Prelle C, Daaboul J (2016) Electromagnetic modular smart surface architecture and control in a microfactory context. Comput Ind 81:152–170. https://doi.org/10.1016/j.compind.2016.02.003

5. Ji Z, Qin S (2022) Bio-inspired smart surface to achieve controllable locomotion through adjustable anisotropic friction. Friction 10:1180–1191. https://doi.org/10.1007/s40544-021-0520-6

6. Bohringer K-F, Donald BR, MacDonald NC (1999) Programmable force fields for distributed manipulation, with applications to mems actuator arrays and vibratory parts feeders. Int J Rob Res 18(2):168–200

7. Will P, Liu W (1994) Parts manipulation on a mems intelligent motion surface. USC INFORMATION SCIENCES INSTITUTE

8. Böhringer K-F, Bhatt V, Donald BR, Goldberg K (2000) Algorithms for sensorless manipulation using a vibrating surface. Algorithmica. https://doi.org/10.1007/s004539910019

9. Frei, P.U., Wiesendanger, M., Büchi, R., Ruf, L.: Simultaneous planar transport of multiple objects on individual trajectories using friction forces. In: Distributed Manipulation, pp. 49–64. Springer, Boston, MA (2000). DOI: 10.1007/978-1-4615-4545-3_3

10. Whiting J, Mayne R, Melhuish C, Adamatzky A (2018) A cilia-inspired closed-loop sensor-actuator array. J Bionic Eng 15:526–532. https://doi.org/10.1007/s42235-018-0043-7

11. Becker KP, Chen Y, Wood RJ (2020) Mechanically programmable dip molding of high aspect ratio soft actuator arrays. Adv Funct Mater 30(12):1908919. https://doi.org/10.1002/adfm.201908919

12. Fantoni G, Santochi M (2010) Development and testing of a brush feeder. CIRP Ann 59(1):17–20. https://doi.org/10.1016/j.cirp.2010.03.049

13. Laurent GJ, Moon H (2015) A survey of non-prehensile pneumatic manipulation surfaces: principles, models and control. Intell Serv Robot 8:151–163. https://doi.org/10.1007/s11370-015-0175-0

14. Chen X, Zhong W, Li C, Fang J, Liu F (2018) Development of a contactless air conveyor system for transporting and positioning planar objects. Micromachines 9(10). https://doi.org/10.3390/mi9100487

15. Chen Z, Deng Z, Dhupia JS, Stommel M, Xu W (2021) Motion modeling and trajectory tracking control for a soft robotic table. IEEE/ASME Trans Mechatronics:1–11. https://doi.org/10.1109/TMECH.2021.3120436

16. Raptis IA, Hansen C, Sinclair MA (2022) Design, modeling, and constraint-compliant control of an autonomous morphing surface for omnidirectional object conveyance. Robotica 40(2):213–233. https://doi.org/10.1017/S0263574721000473

17. Huayu, W., Shunsuke, Y., Shuji, T.: Fabrication of multi-axis moving coil type electromagnetic micro-actuator using parylene beams for pure in-plane motion. In: 2021 21st International Conference on Solid-State Sensors, Actuators and Microsystems (Transducers), pp. 667–670 (2021). DOI: https://doi.org/10.1109/Transducers50396.2021.9495590

18. Tisnés SD, Petit L, Prelle C, Lamarque F (2021) Modeling and experimental validation of a planar microconveyor based on a 2 × 2 array of digital electromagnetic actuators. IEEE/ASME Trans Mechatronics 26(3):1422–1432. https://doi.org/10.1109/TMECH.2020.3020331

19. Rizescu CI, Pleşea AI, Rizescu D (2021) Modular transport and sorting system with omnidirectional wheels. MATEC Web Conf. https://doi.org/10.1051/matecconf/202134308011

20. Keek JS, Loh SL, Chong SH (2021) Design and control system setup of an e-pattern omniwheeledcellular conveyor. Machines. https://doi.org/10.3390/machines9020043

21. Böhringer KF (1997) Programmable force fields for distributed manipulation, and their implementation using micro-fabricated actuator arrays. PhD thesis, Cornell University

22. Zeggari R, Yahiaoui R, Malapert J, Manceau J-F (2010) Design and fabrication of a new two-dimensional pneumatic micro-conveyor. Sens Actuator A Phys 164:125–130. https://doi.org/10.1016/j.sna.2010.09.013

23. Ku, P.-J., Winther, K.T., Stephanou, H.F., Safaric, R.: Distributed control system for an active surface device. In: Proceedings 2001 ICRA. IEEE International Conference on Robotics and Automation (Cat. No.01CH37164), vol. 4, pp. 3417– 34224 (2001). DOI: 10.1109/ROBOT.2001.933146

24. Bhattacharjee A, Lu YT, Becker A, Kim M (2021) Magnetically controlled modular cubes with reconfigurable self-assembly and disassembly. IEEE Trans Robot:1–13. https://doi.org/10.1109/TRO.2021.3114607

25. Tao, S., Youpan, Z., Hui, Z., Pei, W., Yongguo, Z., Guangliang, L.: Three-wheel driven omnidirectional reconfigurable conveyor belt design. In: 2019 Chinese Automation Congress (CAC), pp. 101–105 (2019). DOI: https://doi.org/10.1109/CAC48633.2019.8997050

26. Sanghai, R.A., Saundalkar, P.P., Mallick, J.A., Shah, B.: Sort x consignment sorter using an omnidirectional wheel array for the logistics industry. In: 2020 International Conference on Convergence to Digital World-Quo Vadis (ICCDW), pp. 1–5 (2020). DOI: https://doi.org/10.1109/ICCDW45521.2020.9318687 . IEEE

27. Krühn, T., Falkenberg, S., Overmeyer, L.: Decentralized control for small-scaled conveyor modules with cellular automata. In: 2010 IEEE International Conference on Automation and Logistics, pp. 237–242 (2010). DOI: https://doi.org/10.1109/ICAL.2010.5585288

28. Overmeyer L, Ventz K, Krühn SF (2010) Interfaced multidirectional small-scaled modules for intralogistics operations. Logist Res. https://doi.org/10.1007/s12159-010-0038-1

29. Bedillion M, Messner W (2013) Trajectory tracking control for actuator arrays. IEEE Trans Control Syst Technol 21(6):2341–2349. https://doi.org/10.1109/TCST.2012.2222408

30. Costanzo, M., Myers, D.H.: Diverting Conveyor with Bidirectional Assist Roller., 2015. US Patent 9,156,629

31. Kleczewski, L.: Weighing and Sorting Roller Belt Conveyor and Associated Method., 2020. US Patent App. 16/640,445

32. He B, Wang S, Liu Y (2019) Underactuated robotics: A review. Int J Adv Robot Syst 16(4):1729881419862164. https://doi.org/10.1177/1729881419862164

33. Bianchi E, Jorg OJ, Fantoni G, Dueso FJB, Yagüe-Fabra JA (2023) Design of a Test Bench to Measure In-plane Friction Forces Produced by a New Underactuated Modular Device. 132 AST:155–164. https://doi.org/10.4028/p-d8PGkS

34. Bianchi E, Jorg OJ, Fantoni G, Brosed Dueso FJ, Yagüe-Fabra JA (2023) Study and simulation of an under-actuated smart surface for material flow handling. Appl Sci 13(3). https://doi.org/10.3390/app13031937

35. The MathWorks. MATLAB documentation set, 2022b version (2022)

36. The MathWorks Inc.: Optimization Toolbox. The MathWorks Inc. (2022)

37. Bouguet, J.-Y.: Camera calibration toolbox for matlab (2022) DOI: https://doi.org/10.22002/D1.20164

38. Olson, E.: Apriltag: A robust and flexible visual fiducial system. In: 2011 IEEE International Conference on Robotics and Automation, pp. 3400–3407 (2011). DOI: https://doi.org/10.1109/ICRA.2011.5979761

39. BIPM, IEC, IFCC, ILAC, ISO, IUPAC, IUPAP, OIML (2008) Evaluation of measurement data — Guide to the expression of uncertainty in measurement. Jt Committee Guides Metrol JCGM 100:2008

40. López, C.P.: MATLAB Optimization Techniques. MATLAB Programming, pp. 23–51. Apress, Berkeley, CA (2014). DOI: 10.1007/978-1-4842-0292-02

41. Piatkowski T, Szempruch J (2011) Ranges of application of sorting manipulators. J Polish CIMAC 6(3):235–244

42. Omnitrack: Omnitrack catalogue. Technical report (2022)